Quantum Simulations and Experimental Insights into Glyphosate Adsorption Using Graphene-Based Nanomaterials

Wanderson S. Araújo, Celso Ricardo Caldeira Rêgo,* Diego Guedes-Sobrinho, Alexandre Cavalheiro Dias, Isadora Rodrigues do Couto, José Rafael Bordin, Carolina Ferreira de Matos, and Maurício Jeomar Piotrowski

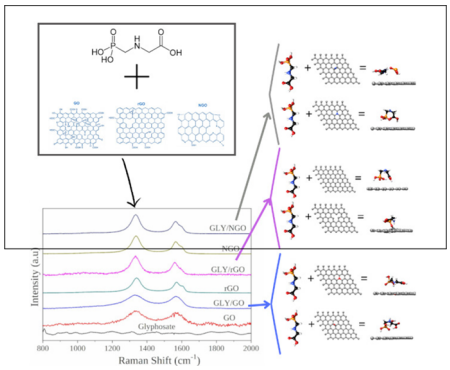

ABSTRACT: The increasing global demand for food and agrarian development brings to light a dual issue concerning the use of substances that are crucial for increasing productivity yet can be harmful to human health and the environment when misused. Herein, we combine insights from high-level quantum simulations and experimental findings to elucidate the fundamental physicochemical mechanisms behind developing graphene-based nanomaterials for the adsorption of emerging contaminants, with a specific focus on pesticide glyphosate (GLY). We conducted a comprehensive theoretical and experimental investigation of graphene-based supports as promising candidates for detecting, sensing, capturing, and removing GLY applications. By combining ab initio molecular dynamics and density functional theory calculations, we explored several chemical environments encountered by GLY during its interaction with graphene-based substrates, including pristine and punctual defect regions. Our results unveiled distinct interaction behaviors: physisorption in pristine and doped graphene regions, chemisorption leading to molecular dissociation in vacancy-type defect regions, and complex transformations involving the capture of N and O atoms from impurity-adsorbed graphene, resulting in the formation of new GLY-derived compounds. The theoretical findings were substantiated by FTIR and Raman spectroscopy, which proposed a mechanism explaining GLY adsorption in graphene-based nanomaterials. The comprehensive evaluation of adsorption energies and associated properties provides valuable insights into the intricate nature of these interactions, shedding light on potential applications and guiding future experimental investigations of graphene-based nanofilters for water decontamination.

KEYWORDS: *density functional theory, graphene, glyphosate, adsorption, spectroscopy*

1. INTRODUCTION

Agriculture, an essential component of human society, is a cornerstone of the economy, playing an undeniable role in supplying raw materials for industry and, more crucially, ensuring food security for humanity. The advancement of agricultural practices and innovations has been instrumental in boosting productivity and facilitating large-scale food production.[1,2] Notably, agricultural pesticides, encompassing chemical, physical, and biological pest, and weed control agents have significantly contributed to this progress.[3] Among these pesticides, one stands out: *N*-(phosphonomethyl)glycine, widely known as glyphosate (GLY). GLY is a nonselective herbicide with broad effectiveness and is among the most widely used pesticides globally for weed control.[4] Unlike other organophosphates targeting the cholinesterase enzyme, GLY primarily inhibits the enzyme 5-enolpyruvyl-shikimate-3-phosphate synthase and exhibits exceptional translocation properties within plants.[4] Since its introduction in the 1970s, GLY has an annual application of approximately 800,000 tons worldwide, with Brazil leading in its usage, particularly in GLY-tolerant soybean cultivation.[5] Brazil's status as the largest consumer of pesticides is evident, with around 118 commercial GLY-based products available.[6] Given the extensive use of GLY and its introduction into the environment through various pathways during manufacturing, application, and postuse disposal, questions about potential effects on both animal and plant health, as well as short- and long-term environmental impacts,[7] underscore the need for studies focused on GLY detection and removal.

The widespread GLY use has led to the emergence of herbicide-resistant weed biotypes, particularly from the Conyza and Digitaria insularis genera.[4] The environmental and health

consequences of GLY's extensive usage, compounded by the lack of rotation of its mechanisms of action, have resulted in issues affecting both fauna and flora and poisoning incidents.[8,9] As an organophosphate herbicide, GLY exhibits high sorption capacity (adsorption + absorption processes) in the soil, interacting via several physical and chemical mechanisms such as van der Waals forces hydrogen bonds, ionic interactions, hydrophobic bonds, and covalent bonds with soil metal oxides.[10] Although GLY degrades in a few days in the soil, it can strongly adsorb onto soil minerals, leading to accumulation and persistence with a long half-life.[11] Furthermore, it may leach into aqueous environments, including underground water reserves[7,12] and surface waters.[13,14] There is ongoing debate regarding the toxicity of GLY and its metabolite aminomethylphosphonic acid (AMPA).[15−17] While certain studies suggest low human toxicity,[18] others emphatically point to serious risks,[15] including mutagenic, carcinogenic, and genotoxic effects even at low doses,[19] as well as fatal consequences in overdose cases.[20] The United States Environmental Protection Agency sets the maximum contaminant level in drinking water at 700 mg/L, yet concentrations up to 105 mg/L have been found in freshwater supplies.[21] Recently, the European Union approved using GLY for an additional 10 years, subject to new conditions and restrictions.[22] Despite these regulations, it is unanimously acknowledged that due to its small, polar, and highly water-soluble nature, indiscriminate GLY use can result in severe environmental impacts, particularly water pollution, classifying it as an emerging contaminant. Therefore, investigations focusing on materials for GLY monitoring, detection, and removal systems are of great significance,[23] and new technologies based on nanomaterials will be essential to combine precision agriculture with environmental protection.[24]

First, there is great relevance in GLY detection process, as it involves monitoring and verifying the presence of acceptable levels of this molecule in the environment and biological samples, assessing potential contamination and toxic effects stemming from its residual accumulation in the food chain.[20] In this sense, the development of analytical procedures for GLY detection and quantification has been substantial, requiring a high degree of selectivity, sensitivity, and accuracy for analyzing low concentrations of analytes. Notably, chromatographic and fluorescence techniques,[25] as well as electrochemical methods, including cyclic voltammetry and its derivatives, have gained prominence due to their cost-effectiveness, high sensitivity, potential for miniaturization, and automation, which could lead to the development of simpler and more portable devices for field measurements and detections.[26] However, electrochemical detection necessitates an electroactive analyte. This criterion poses a challenge for GLY detection since it does not undergo a redox reaction within the applied potential range, making voltammetric detection unfeasible. Nevertheless, GLY detection can be accomplished through various approaches, including electrode surface modifications, sample treatments, or indirect detection by forming coordination compounds. This often involves using carbon electrodes with metals like copper and gold.[26,27] Nonetheless, there is still a need for further insights to explore the possibilities of harmonizing specific materials with molecules like GLY. Here, the study of systems based on graphene,[27] whether in its pure (pristine) form or when functionalized with vacancies, doping, or heteroatoms, offers potential. Such modifications have the potential to enhance reactivity for molecular interactions and contribute to the feasibility of the sensing and detection process.[28]

Regarding experimental processes for removing emerging contaminants, adsorption emerges as a standout method due to its simplicity, low adsorbent costs, flexibility, and high efficiency.[29] In the case of GLY removal by adsorption to mitigate pollution effects, several materials have been studied, including biochar, zeolites, hydroxides, and various carbon-based materials.[29−31] For graphene-based materials, GLY adsorption typically occurs under low pH conditions, with the protonated phosphate functional group, making it a potent electrophile capable of interacting with the aromatic groups of the adsorbent, thus characterizing chemisorption.[32,33] However, other types of interactions are also feasible.[34] In this context, carbon-based nanomaterials appear as very promising candidates for adsorption due to their remarkable reactivity and chemical selectivity.[31] Among them, special emphasis is given to graphene, which is a two-dimensional material formed by a single layer of carbon atoms organized in planar hexagonal rings, renowned for its exceptional mechanical, electrical, thermal, and optical properties, not to mention its extensive surface area.[28] Isolated in 2004,[35] graphene and its composites have been extensively studied for water treatment. This is owing to their significant surface area, catalytic effects, adsorptive capacity, and reactivity, particularly in the purification and detection of contaminants.[33,36]

However, the graphene used in device construction, such as contaminant gas sensors, has its limitations and is successful only for certain molecules capable of inducing significant changes in the system's conductance during molecular adsorption.[37] Limitations arise when molecules to be detected display weak adsorption characteristics on the graphene surface. This is a common occurrence due to graphene's low inherent reactivity, resulting in relatively weak molecular interactions (physisorption). A viable solution to address this issue is the functionalization of two-dimensional materials like graphene.[28] Incorporating heteroatoms into graphene is particularly relevant, as it enables the merging of properties from both systems, potentially leading to new or enhanced characteristics in the functionalized system.[38,39] Graphene support provides stability to the system. In contrast, heteroatoms can introduce the chemical activity required for effective substrate interaction. Consequently, both pristine graphene and graphene with point defects, including vacancies and heteroatoms (either adsorbed or substitutional),[38] can serve as promising candidates for adsorbing pollutants like GLY, emphasizing the need for further research in this area.[28] With an increasing emphasis on combining graphene, known for its stability, with magnetic elements or nanoparticles, aiming to facilitate phase separation in aqueous solutions by applying magnetic fields.[40,41] Despite that, there remains a scarcity of studies exploring the details of the molecular adsorption effects on sensor systems, and further, research is warranted to expand our understanding.

Thus, in the present work, we investigated the theoretical and experimental GLY behavior in interaction with graphene and its various functionalizations to advance the understanding of the molecular adsorption process in line with experimental results. This investigation encompassed GLY on pristine graphene (PRG), graphene with monovacancy (MVG), graphene with O- and N-doped atoms (ODG and NDG, respectively), and graphene with O- and N-adsorbed atoms (OAG and NAG, respectively). We employed state-of-the-art

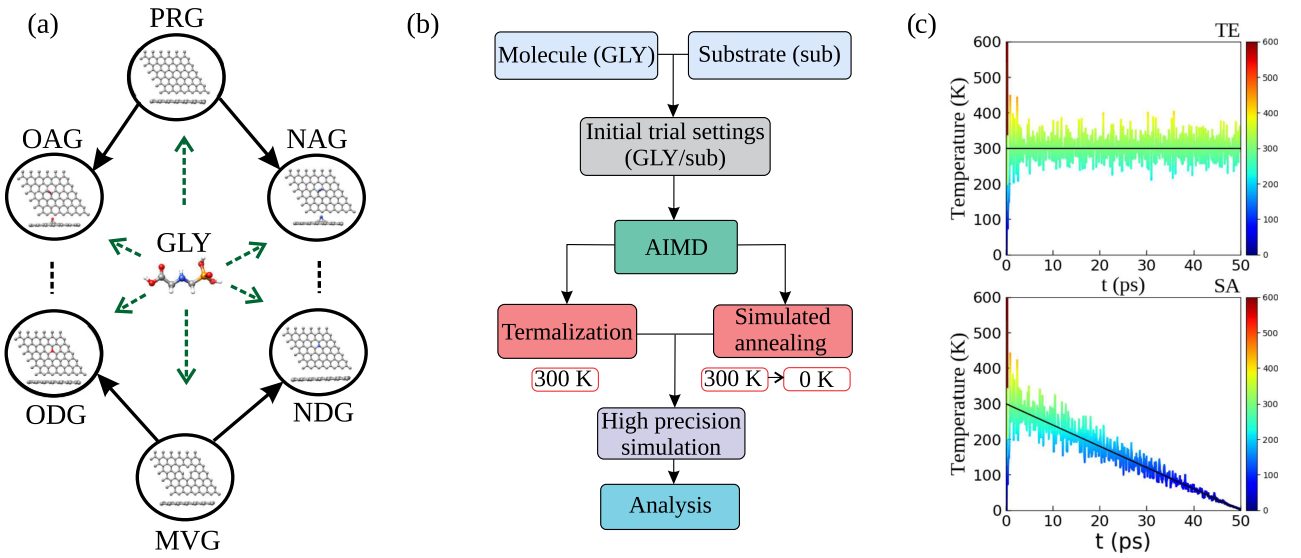

Figure 1. (a) Schematic representation for the GLY and its potential substrates, including PRG, MVG, ODG, NDG, OAG, and NAG. (b) Methodological flowchart for the adsorption process protocol. (c) Temperature (T in K) versus time (t in ps) for the AIMD thermalization (TE) and simulated annealing (SA) exemplification process for GLY/PRG (see Figure S2 in SI for other GLY/subsystems).

quantum-mechanical computational methods with experimental support to address fundamental questions regarding atomistic interactions. Specifically, we conducted first-principles calculations based on density functional theory (DFT) and Ab Initio Molecular Dynamics (AIMD) simulations. Our study aims to provide insights into the interactions within these systems, shedding light on the possibilities of modifying graphene to enhance its capabilities as a sensor and a potential agent for GLY removal. We also investigate the atomistic mechanisms governing the interaction between molecules and substrates and the resulting experimental implications. Our findings contribute to understanding GLY-graphene interactions and can potentially guide the development of future graphene-based nanomaterials for GLY detection and adsorption. The structure of this paper is organized as follows: Section 2 outlines our computational and experimental methods, while Section 3 presents our results and discussion. Finally, Section 4 summarizes our conclusions.

2. METHODOLOGY

2.1. Computational Methods. *2.1.1. Atomic Configurations.* Here, we have considered the interaction limit of a single molecule with a substrate that provides sufficient surface area, which is usually performed at the atomic level and based on graphite and graphene models.[42−44] Consequently, the surface region encountered by the analyte (GLY) in the adsorption process can be composed by six possible constitutions: sub = PRG, MVG, ODG, NDG, OAG, and NAG, as illustrated in Figure 1a. Our substrate models are primarily based on single-layer graphene, as we have observed similar adsorption behavior when using substrates with multiple layers (see Figure S1 in the Supporting Information (SI) material). In this context, we assume a chemical scenario where GLY, in neutral charge state, can interact with several chemical environments, which may involve pure graphene and graphene with punctual defects. These defects are commonly expected in the production of graphene-based nanomaterials.[28,38]

The graphene-based substrates were initially constructed considering the adequate lattice parameters, which were determined accurately by establishing the C−C bond length, ensuring the reproducibility of fundamental properties, and conducting convergence tests (additional details are available in the SI, Tables S1−S4). These methodological tests were crucial to ensure the correct application of the supercell approximation. This includes determining the appropriate substrate dimensions, specifically supercell sizes large enough to accommodate the GLY maximum dimensions while maintaining sufficient separation to prevent interactions between molecular periodic images (punctual defects). The periodic distances of the substrates were defined in the xy plane using (6 × 6) supercells (in comparison with (8 × 8) supercells, see Figure S1), while the nonperiodic direction extended along the z-axis. To prevent interactions between the molecule and substrate periodic images along the z-axis, a vacuum distance ranging from 17 to 20 Å was maintained.

We explored the GLY/sub potential energy surface (PES) for the molecular adsorption stage, considering one molecule per supercell, to find each substrate's most stable adsorbed configuration. To this purpose, we employed a strategy based on AIMD simulations, which is outlined in Figure 1b. Initial trial settings, composed by GLY in arbitrary orientations on graphene substrates, underwent AIMD simulations, incorporating thermalization (TE) at 300 K and simulated annealing (SA) processes (from 300 to 0 K). Both procedures provided sufficient thermal energy to thoroughly explore the PES, identifying various adsorption sites and generating numerous snapshots. The key distinction lies in the temperature reduction during simulated annealing, which allows atoms to freeze in their equilibrium positions. Subsequently, we optimized the final and snapshot AIMD configurations through high-level quantum-mechanical calculations. After a checking process, we analyzed the resulting configurations.

2.1.2. Computational Details. All systems were studied using spin-polarized DFT[45,46] framework within the semilocal exchange-correlation functional based on the generalized gradient approximation proposed by Perdew−Burke−Ernzerhof[47] (PBE). Recognizing the significant role that attractive

nonlocal long-range van der Waals (vdW) interactions can play in describing analyte-substrate interactions,[48,49] we employed the semiempirical vdW D3 correction.[50] This correction added an extra dispersion energy contribution to the total energy within the DFT-PBE framework.

To solve the Kohn−Sham equations, we employed the all-electron projected augmented wave (PAW)[51] method as implemented in the Vienna Ab Initio Simulation Package[52,53] (VASP). This method describes core electrons using fully relativistic calculations, while valence electrons are approximated using a scalar-relativistic approximation.[54] Our calculations utilized a plane-wave cutoff energy of 600 eV, which exceeded the largest recommended cutoff energy (ENMAX) by 50% among the selected PAW files. We also employed a 4 × 4 × 1 **k**-mesh for Brillouin zone integration, generated using the Monkhorst−Pack scheme, and applied a small Gaussian smearing parameter of 1 meV. This parameter is necessary to prevent fractional occupation of electronic states. Equilibrium geometries were attained when atomic forces on each atom reached values smaller than 0.015 eV $Å^{-1}$. We considered a total energy convergence threshold of 1.0×10^{-6} eV for electron density self-consistency. For our AIMD simulations, we employed the Nosé algorithm, with both the TE and SA processes running for 50 ps each. A time step of 1 fs was used to generate several adsorbed snapshots.

2.2. Experimental Methods. For comparison with theoretical calculations, three graphene species were utilized in the experimental part: (i) graphene oxide (GO), (ii) reduced graphene oxide (rGO), and (iii) reduced graphene oxide doped with nitrogen (NGO). The expected chemical structures of these graphene species are illustrated in Figure S3. Structurally, GO primarily resembles oxygen-containing substrates (ODG and OAG). However, it is important to note that due to its high oxidation, GO exhibits numerous vacancies and can be likened to MVG. On the other hand, rGO structurally resembles PRG, but it is important to highlight the presence of vacancies and residual functional groups. Lastly, NGO is more akin to nitrogen-doped graphene (NDG) and at a lower comparison factor with nitrogen-adsorbed graphene (NAG).

Graphene oxide and reduced graphene oxide were synthesized through a chemical oxidation method of graphite. The GO reduction to rGO was achieved using sodium borohydride ($NaBH_4$) from Merck.[55] Nitrogen incorporation into graphene oxide followed the procedure proposed by Sun and collaborators.[56] Deionized water obtained through a Milli-Q system was used throughout the experiments. The GLY adsorption was carried out at room temperature and pH of 7 by mixing 100 mg of each graphene material with 10 mL of a commercial GLY solution (PESTANAL, 100 mg/L) and stirring for 24 h. Subsequently, the graphene substrates were filtered and dried in an oven at 60 °C for 24 h. Analysis of the graphene materials before and after adsorption and the GLY was conducted using a Vertex-70 (Bruker) in attenuated total reflectance (ATR) mode with an ATR accessory from Pike Technologies. Raman spectra were obtained using a SENTERRA confocal Raman microscope (Bruker) with a 532 nm laser.

Finally, it is important to highlight that our work focuses mainly on the mechanisms of GLY adsorption on graphene substrates, without a specific focus on degradation.

3. RESULTS AND DISCUSSION

3.1. Theoretical Results. *3.1.1. Analyte and Substrates.* The individual systems, GLY and substrates, are depicted in Figure 1a. Additional details, including top and side views, along with the corresponding binding energy (E_b) values, are provided in Figure S4. E_b serves as a measure of energy stability and is calculated by subtracting the total energy of the system (molecule or substrates) from the total energies of the free atoms that make up that respective system. Negative E_b values are given per atom and indicate the energetic stability of system formation, as per the adopted definition. GLY, a phosphonate from the organophosphorus compound family, is a stable and nonmagnetic molecule with an E_b of −4.383 eV per atom. The structural and vibrational results are in excellent agreement with previous works.[57,58] GLY possesses three polar functional groups − amine, carboxylate, and phosphonate − imparting characteristics such as high water solubility, strong adhesion to soil constituents, and charge variability in response to soil pH.[59]

Graphene-based substrates were derived from PRG and its variants; for instance, OAG and NAG were created by adsorbing O and N adatoms on PRG, respectively. Adsorption tests were conducted on top, bridge, and hollow sites, with structural optimizations revealing the bridge site as the most stable for both cases. The MVG substrate was generated by removing a single C atom from PRG, leading to at least three different monovacancy configurations. These configurations are determined by the distances and disposition of C atoms in the vacancy region and the total magnetic moment (m_T) values of the system. Three distinct monovacancy configurations emerged: a nonsymmetric single vacancy resulting in a metastable nonmagnetic configuration featuring an out-of-plane C atom, a planar and symmetric configuration, and the most stable MVG configuration (used in our study). The latter exhibits symmetry reduction, with one of the C−C distances (1.98 Å) being smaller than the other two (2.55 Å), accompanied by m_T = 1.5 μ_B, in excellent agreement with previous studies.[44,60] From the MVG substrate, we constructed ODG and NDG configurations, where O and N atoms were adsorbed near the vacancy region. The most stable results were obtained when O and N atoms became substitutional, occupying the removed C atom position. In Table 1 are shown the E_b and m_T properties for the graphene-based substrates.

Table 1. Binding Energy, E_b (in eV Per Atom), and Total Magnetic Moment, m_T (in μ_B), Values for the PRG, MVG, NDG, ODG, NAG, and OAG Substrates

	PRG	MVG	NDG	ODG	NAG	OAG
E_b	−7.876	−7.768	−7.827	−7.768	−7.781	−7.798
m_T	0.000	1.500	0.000	0.000	0.000	0.000

From Table 1, we observe negative E_b values indicating energetic stability for all substrates. There is a slight preference for PRG, followed by NDG, OAG, NAG, ODG, and MVG, resulting in a statistically slightly greater probability of PRG configuration-type formation in graphene-based substrates. However, depending on the experimental aspects involved in substrate construction, such as reagent purity, handling, and the chemical environment of the reaction, it is feasible to find punctual defects. This is due to the small relative binding

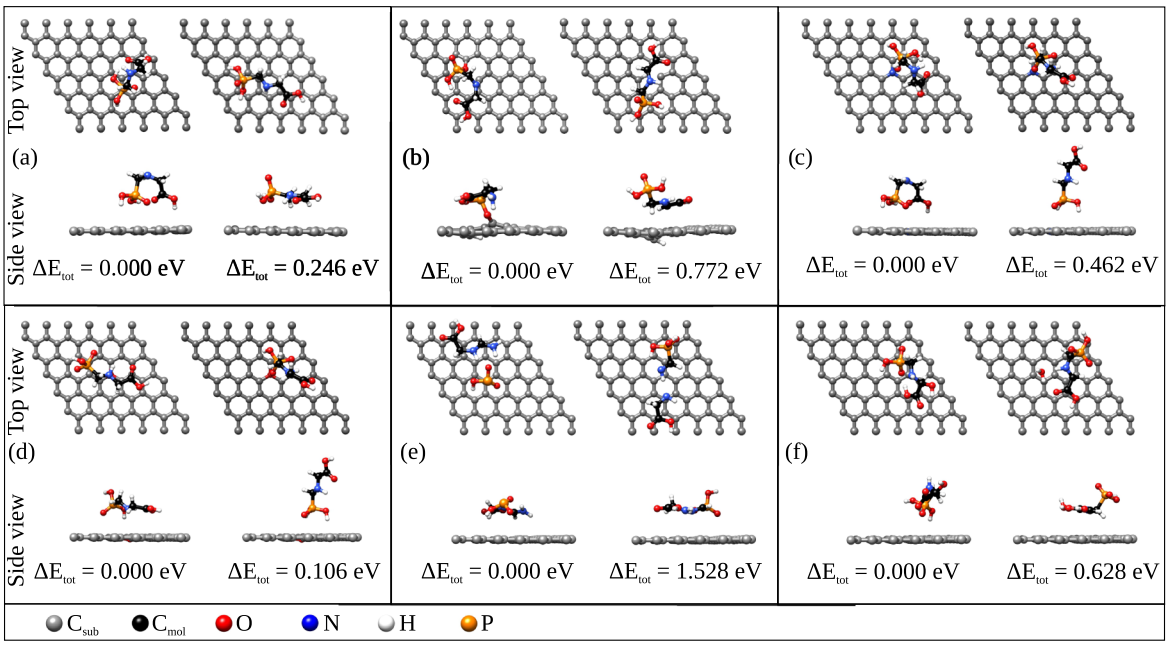

Figure 2. Top and side views of two representative conformations, including the lowest energy configuration, are presented for the following systems: (a) GLY/PRG, (b) GLY/MVG, (c) GLY/NDG, (d) GLY/ODG, (e) GLY/NAG, and (f) GLY/OAG. Additionally, the relative total energy (ΔE_{tot}), in relation to the lowest energy conformation (0.000 eV), is depicted for each set.

energy difference, changing between ≈0.05 eV/atom (NDG−PRG) and 0.11 eV/atom (MVG−PRG). The PRG substrate exhibits standard characteristics of a two-dimensional hexagonal lattice, including planarity and absence of magnetism, as reported in the literature.[44,61] It has an equilibrium lattice parameter of 2.461 Å, corresponding to an average C−C bond length of 1.421 Å and exact coordination number of 3.

The punctual defect configurations exhibit a smaller E_b magnitude compared to PRG, implying higher reactivity. For instance, the MVG configuration demonstrates increased reactivity and lower stability attributed to unsaturated dangling bonds.[44] The monovacancy formation energy is estimated using $E_{vac} = E_{tot}^{MVG} - (n-1)/nE_{tot}^{PRG}$, where n is the number of C atoms in PRG. The calculated value is 7.711 eV, aligning with both experimental[62] and theoretical[44] results. Among all the supports investigated, MVG is the only configuration exhibiting magnetism. This magnetic property is induced by the single vacancy, which disrupts the symmetry of the π-electrons.

The doped configurations (NDG and ODG) have the missing bonds in the vacancy region remedied by adatoms (N or O), resulting in a zero m_T. We can estimate the doping energy using $E_{dop} = E_{tot}^{NDG\ or\ ODG} - E_{tot}^{MVG} - E_{tot}^{N\ or\ O\ free\text{-}atom}$). The obtained values are −12.061 and −7.821 eV, with C−N and C−O average bond lengths of 1.408 and 1.484 Å for NDG and ODG substrates, respectively, both in-plane. Similarly, the N and O adsorbed configurations (NAG and OAG) exhibit null total magnetic moments. In contrast to the doped configurations, which display large E_{dop} magnitudes, the adsorbed configurations show lower adsorption energy values ($E_{ad} = E_{tot}^{NDG\ or\ ODG} - E_{tot}^{PRG} - E_{tot}^{N\ or\ O\ free\text{-}atom}$) at −0.955 and −2.158 eV, respectively. The higher PRG stability can explain this compared to MVG. The average bond distances between C−N and C−O are 1.464 and 1.465 Å, respectively, both out-of-plane. The values presented for two sets of graphene systems with N and O atoms agree with the literature.[63,64]

3.1.2. Analyte−Substrate Stability. After conducting individual characterizations of the systems (analyte and substrates), we proceeded with the molecular adsorption process involving analyte−substrate interactions. As illustrated in our model (Figure 1), each GLY molecule can exist in six potential chemical environments, namely, GLY/PRG, GLY/MVG, GLY/NDG, GLY/ODG, GLY/NAG, and GLY/OAG. Despite the limited number of substrates, there is a considerable variety of possible interaction modes. In fact, Figure S5 illustrates the electrostatic potential map of each of the six possible substrates, providing a qualitative glimpse of the changes in the potential energy surface experienced by the adsorbate. To encompass the full spectrum of PES scenarios, we employed our AIMD-based strategy. Figure 2 showcases the most stable configurations for each case compared to a nonequivalent configuration of interest. Additionally, in the SI (Figures S6−S11), we provide the five most stable and nonequivalent configurations for each substrate, along with their respective relative total energies: $\Delta E_{tot} = E_{tot}^{i} - E_{tot}^{low}$, where E_{tot}^{i} and E_{tot}^{low} represent the total energies for a given configuration i and the lowest energy configuration (low), respectively. The most stable conformations for each analyte−substrate system (0.000 eV) are the most likely to be obtained in an experimental situation. However, they are not the only possibilities within an energy window.

For GLY/PRG (Figure 2a), we observe the analyte interacting with the substrate in a horizontal orientation, adopting a twisted molecular conformation. This conformation positions the carboxylic and phosphonic groups in close interaction with the substrate surface while distancing the amine group. Comparatively, the untwisted molecule, arranged horizontally on the substrate, is 0.246 eV less stable. Figure S6 presents additional orientations of the GLY molecule on the substrate, revealing only a slight difference in relative total energy (approximately 0.302 eV). This small energy disparity underscores the potential coexistence of different orientations within the PRG chemical environment.

In Figure 2b, the GLY/MVG scenario is different. The heightened reactivity of the substrate, attributed to the monovacancy, intensifies the interaction with the analyte. This is evident in the dissociation of the molecule. In the most stable conformation (0.000 eV), a H atom is lost from the phosphonic group, binding to one of the low-coordinated C atoms in the vacancy region. Simultaneously, the analyte chemically bonds to the substrate via an O atom (which lost the hydrogen), forming a C−O bond between GLY and MVG. An alternative conformation highlighted in Figure 2b depicts a scenario where the interaction bypasses the phosphonic group. In this instance, we observe a decrease in stability (0.772 eV). Despite one of the CH_2 groups losing a H atom to the substrate, a strong interaction fails to establish a chemical bond.

Most lower-energy snapshots arising from the GLY−MVG interaction validate conformations like the most stable one. In this predominant scenario, a H atom is lost from the molecule's phosphonic group to the substrate's vacancy region, culminating in the subsequent formation of a C−O chemical bond between GLY and MVG. This pattern is evident in the three most stable conformations showcased in Figure S7. Configurations resulting from the interplay of the vacancy with other molecule functional groups, while capable of capturing a H atom, exhibit lower stability. For instance, the interaction with the carboxylic group also leads to the formation of a C−O chemical bond between GLY and MVG but is less stable (0.989 eV).

In Figure 2c,d, we examine the GLY/NDG and GLY/ODG cases, respectively. The substitutional N or O atoms (replacing the removed C atom) result in decreased reactivity with the substrate. From Figure 2c, the most stable GLY/NDG conformation (0.000 eV) mirrors that of GLY/PRG, where the molecule interacts horizontally with the substrate, undergoing a twist that brings the carboxylic and phosphonic groups closer to the substrate surface. Another highlighted conformation in Figure 2c reveals a decrease in stability (0.462 eV) for interactions with the molecule positioned vertically in relation to the substrate. Conversely, in Figure S8, we illustrate that bringing the molecule closer to the amine group decreases the stability of the systems by approximately 0.305 eV. Furthermore, it also demonstrates the independence of the molecule's positioning on the substrate, indicating energetically degenerate configurations both in the doping region and away from it (Figure S8b,c, respectively).

In Figure 2d, the most stable GLY/ODG conformation (0.000 eV) exhibits a horizontal parallel interaction over the doping region, with minimal distortions in the GLY molecule. Notably, the second highlighted structure in Figure 2d positions the molecule vertically. Unlike the GLY/NDG case, the relative energy is more than four times lower (0.106 eV), indicating that the proximity between the doping region of the substrate and the analyte via O atoms of the phosphonic group results in an energy gain. Figure S9 further illustrates that different orientational conformations of the molecule on the substrate yield configurations with closely matched energies, with relative total energies lower than 0.280 eV.

In Figure 2e,f, distinct scenarios unfold for the GLY/NAG and GLY/OAG cases, respectively. Introducing adsorbed N or O atoms keeps lower reactivity to the substrate. Still, this alteration induces changes in the molecule itself, resulting in configurations with lower energy. In Figure 2e, the most stable GLY/NAG conformation (0.000 eV) arises from a situation where GLY appropriates the N atom previously adsorbed on the substrate. This leads to the formation of a molecular compound, $HO_3P\cdots C_3H_7N_2O_2$, featuring two radicals interacting via hydrogen bonds (O···2H). Another highlighted conformation in Figure 2e depicts the formation of a different double radical molecular compound, $CH_3NO_2P\cdots C_2H_4NO_2$, with interaction via a hydrogen bond (N···H). However, this configuration is 1.528 eV less stable. Figure S10 illustrates that configurations where N is not appropriated by GLY exhibit significantly lower stability, ranging between 2.996 and 3.511 eV.

In Figure 2f, the most stable GLY/OAG conformation (0.000 eV) arises from a scenario where GLY appropriates the O atom previously adsorbed on the substrate. This results in the formation of a distorted $C_3H_8NO_6P$ molecular compound (approximating the phosphonic and carboxylic groups), now featuring an additional hydroxyl radical. Another highlighted conformation in Figure 2f demonstrates that capturing the O atom from the substrate, albeit incurring an energetic cost of 0.628 eV, facilitates the transformation of the GLY molecule into $C_3H_6NO_5P \cdots H_2O$, once again interacting via hydrogen bonds. Similar to the GLY/NAG case, Figure S11 illustrates that configurations where the O atom is not appropriated by the molecule exhibit significantly lower stability, ranging between 2.740 and 3.006 eV.

It is essential to highlight that while we have presented cases where there is molecular dissociation (GLY/MVG) and chemical transformation of GLY into other species (GLY/NAG and GLY/OAG) as spontaneous, we must emphasize that they were obtained under specific temperature conditions. In other words, the configurations resulting from the optimization calculations were obtained from AIMD simulations via TE or SA processes (see the Computational Methods subsection).

3.1.3. Analyte−Substrate Interaction. Considering the lowest energy GLY/sub configurations (0.000 eV), we computed key properties associated with the GLY−sub interaction, encompassing the adsorption energy (E_{ad}), the minimum distance between GLY and sub after adsorption ($d_{min}^{GLY\text{-}sub}$), the effective Bader charges (q^{GLY} and q^{sub}), the percentage variations in the bond lengths of the molecule (Δd_{av}^{GLY}) and the substrate (Δd_{av}^{sub}), and, finally, the total magnetic moment (m_T) of the systems.

For E_{ad}, we have extended beyond the conventional definition, which typically considers the interacting system in relation to separate systems. In this context, we define E_{ad} as the sum of the interaction energy (E_{int}) and the respective distortion energies (E_{dist}^{GLY} and E_{dist}^{sub}) of its constituents due to the interaction, as expressed in the following equation:[44]

$$\begin{aligned} E_{ad} &= E_{tot}^{GLY/sub} - E_{tot}^{GLY\ relaxed} - E_{tot}^{sub\ relaxed} \\ &= E_{int} + E_{dist}^{GLY} + E_{dist}^{sub} \end{aligned} \quad (1)$$

where $E_{tot}^{GLY/sub}$, $E_{tot}^{GLY\ relaxed}$, and $E_{tot}^{sub\ relaxed}$ represent the total energies of GLY/sub, isolated, and relaxed GLY and sub, respectively. Additionally, the E_{int}, E_{dist}^{GLY}, and E_{dist}^{sub} terms are defined as follows: $E_{int} = E_{tot}^{GLY/sub} - E_{tot}^{GLY\ frozen} - E_{tot}^{sub\ frozen}$; $E_{dist}^{GLY} = E_{tot}^{GLY\ frozen} - E_{tot}^{GLY\ relaxed}$; and $E_{dist}^{sub} = E_{tot}^{sub\ frozen} - E_{tot}^{sub\ relaxed}$. Here, $E_{tot}^{GLY\ frozen}$ and $E_{tot}^{sub\ frozen}$ represent the total energies calculated from the frozen structures obtained from the GLY/subsystems in equilibrium.

Our approach involves the decoupling of the GLY−sub interaction by decomposing the adsorption energy into an

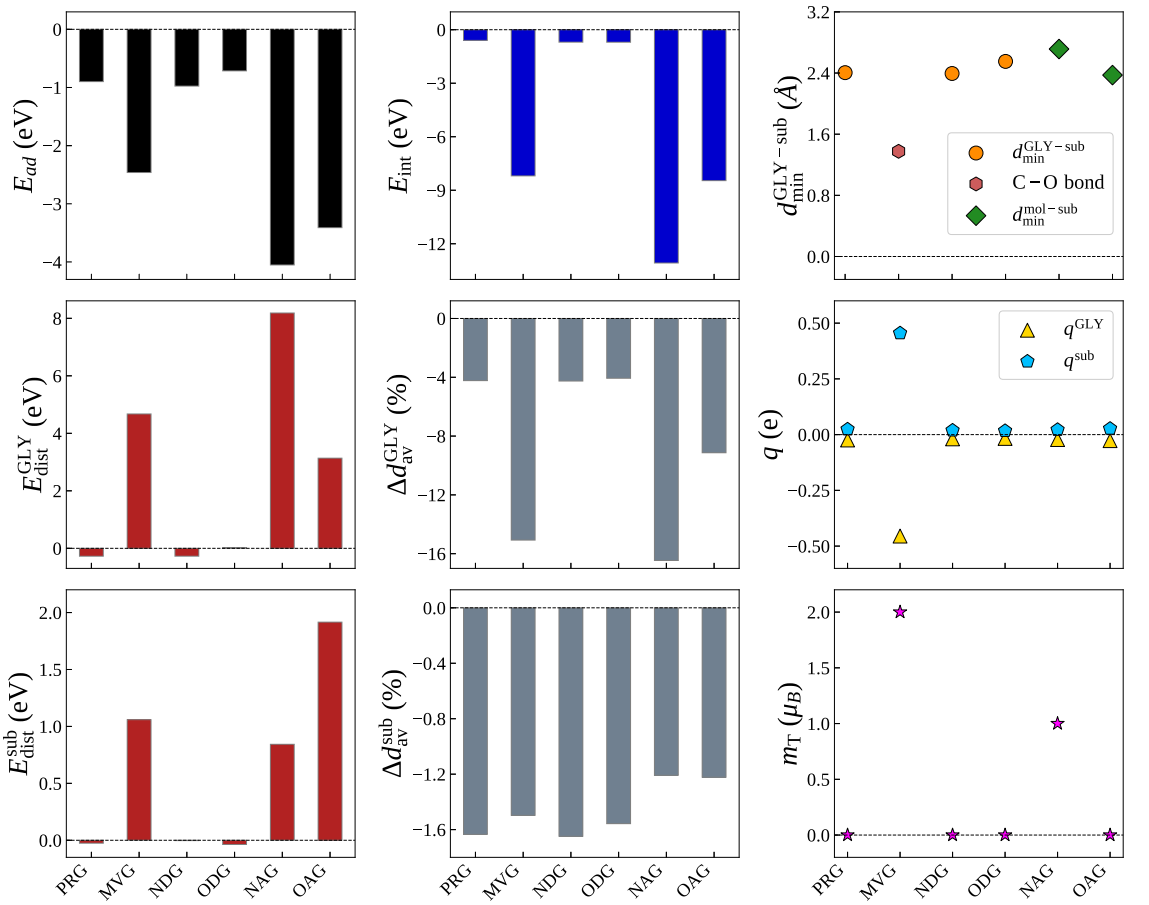

Figure 3. Main adsorption properties for the lowest energy GLY/sub (sub = PRG, MVG, NDG, ODG, NAG, and OAG) systems: adsorption energy (E_{ad}), interaction energy (E_{int}), distortion energies (E_{dist}^{GLY} and E_{dist}^{sub}), minimum bond length distances between GLY and sub ($d_{min}^{GLY-sub}$), the relative deviation for the average bond lengths (Δd_{av}^{GLY} and Δd_{av}^{sub}), effective Bader charges (q^{GLY} and q^{sub}), and the total magnetic moments (m_T).

additive term (E_{int}) and two nonadditive terms (E_{dist}^{GLY} and E_{dist}^{sub}). A comprehensive understanding of the analyte−substrate interaction is achieved by measuring (i) the interaction between the systems through E_{int} and $d_{min}^{GLY-sub}$, (ii) the modifications/deformations experienced by individual systems during interaction, and (iii) the energetic and structural penalties from can be estimated using E_{dist}^{GLY} and E_{dist}^{sub} for the energetic part and through Δd_{av}^{GLY} and Δd_{av}^{sub} for the structural part. These latter terms are defined by the structural changes in average bond lengths after adsorption (ads) in relation to the respective separate systems before adsorption, as expressed in eq 2:

$$\Delta d_{av} = \frac{(d_{av,ads} - d_{av}) \times 100}{d_{av}} \quad (2)$$

Finally, the characterization of the charge variations due to the GLY−sub interaction is given by the q^{GLY} and q^{sub} values. At the same time, electronic changes manifested in magnetic properties can be ascertained through m_T. Figure 3 and Table S5 present the key property values for the lowest energy configurations.

The properties presented in Figure 3 (Table S5) reveal negative E_{ad} values, indicating the energetically favorable interaction of GLY with graphene-based substrates. Three primary interaction behaviors emerge (**1**) When GLY encounters regions of pristine graphene (GLY/PRG) or punctual defects based on N- and O-dopings (GLY/NDG, GLY/ODG), physisorption occurs. In this case, the molecule interacts horizontally with the substrates. (**2**) GLY/MVG exhibits chemisorption when encountering vacancy-type defect regions on graphene. This results in a strong analyte−substrate interaction, leading to partial molecule dissociation. This interaction can potentially lead to substrate poisoning by atomic species from the molecule and binding the molecule to the substrate. (**3**) When GLY encounters graphene regions with punctual defects based on N and O adsorptions (GLY/NAG, GLY/OAG), the atomic species adsorbed on the substrate are captured by the molecule. This leads to the formation of new chemical compounds, such as derivatives of phosphates, glycines, phosphoserines, and water.

In case (**1**), greater dispersive contributions characterize the GLY-substrate physisorption interaction. The E_{ad} magnitudes are relatively small, measuring −0.899 eV for GLY/PRG, −0.976 eV for GLY/NDG, and −0.714 eV for GLY/ODG. Additionally, the $d_{min}^{GLY-sub}$ values are larger at 2.405 Å, 2.394 Å, and 2.552 Å, respectively, indicating a typical distance between the analyte and substrate for physisorbed systems. Furthermore, the molecular interaction in physisorbed systems does not significantly alter the preexisting magnetic behavior. The isolated GLY, PRG, NDG, and ODG systems exhibit nonmagnetic characteristics, and after the adsorption process, they maintain a total magnetic moment of zero for all conformations. This observation aligns with the reported weak adsorbate−substrate interaction. Moreover, these findings are consistent with the nonsignificant charge transfers between

GLY and the respective substrates observed throughout the interaction, as exemplified for GLY/PRG in Figure 4a and for the other systems in Figure S12.

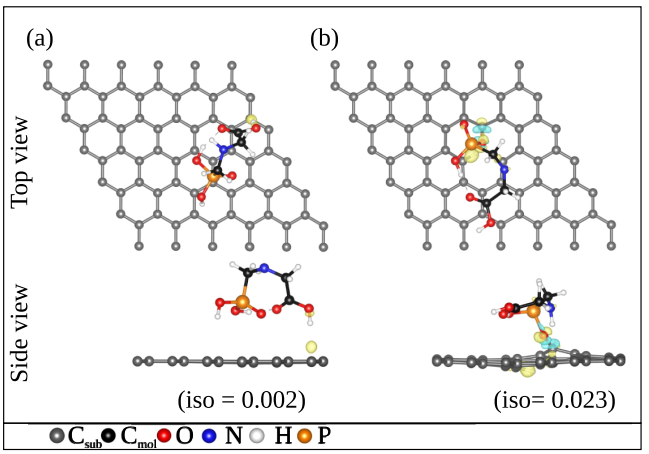

Figure 4. Top and side views of the charge density difference plots for the lowest energy (a) GLY/PRG and (b) GLY/MVG configurations. Isosurface (iso) values are shown in the figure, with cyan and yellow colors representing charge depletion and accumulation, respectively.

The trend observed in case (**1**) is manifested in the E_{ad} decomposition, where a higher contribution from E_{int} is evident compared to E_{dist}^{GLY} and E_{dist}^{sub}. Specifically, for GLY/PRG and GLY/NDG (GLY/ODG), approximately 66.5 and 71.6% (98.3%) of the adsorption energy originates from the interaction energy, with an additive (nonadditive) contribution from molecular distortion accounting for 30.6 and 28.1% (3.5%). Meanwhile, there are minor energy contributions due to substrate distortion: 2.9 and 0.3% (5.2%), respectively. This finding aligns seamlessly with the observed relative deviation for Δd_{av}^{GLY} and Δd_{av}^{sub} values. The results underscore the earlier observation that the molecule undergoes a twist in the more stable GLY/PRG and GLY/NDG systems, bringing the carboxylic and phosphonic groups closer together. At the same time, such distortion is absent in GLY/ODG.

In case (**2**), the most stable GLY/MVG configuration exhibits a higher E_{ad} magnitude compared to case (**1**), with an estimated value of ≈−2.462 eV. This increase is attributed to the high reactivity of the vacancy region, resulting in molecular dissociation and local substrate deformation. The GLY dissociation involves the loss of a H atom, subsequently incorporated into a monovacancy site. Additionally, a C−O chemical bond forms between the dissociated GLY and another substrate vacancy site, resulting in $d_{min}^{GLY\text{-}MVG}$ assuming the C−O bond distance value, i.e., 1.376 Å. Consequently, molecular dissociation and analyte-substrate coupling represent a scenario of increased stabilization for the entire system.

The E_{ad} decomposition reveals a substantial E_{int} magnitude (≈−8.195 eV), accompanied by significant penalties for molecular dissociation (≈4.674 eV) and local substrate deformation (1.059 eV). These energetic results align closely with the observed structural changes induced by the GLY-MVG interaction, reflected in Δd_{av}^{GLY} (−15.08%) and Δd_{av}^{MVG} (−1.50%). The energetic and structural findings are consistently linked to the charge transfer process, as evidenced by our Bader charge analysis and charge density difference plots (Figure 4b). Specifically, GLY receives (−0.455 *e*) while MVG donates (0.455 *e*) charge. Lastly, the contributions of molecular dissociation and the GLY-MVG bond result in an

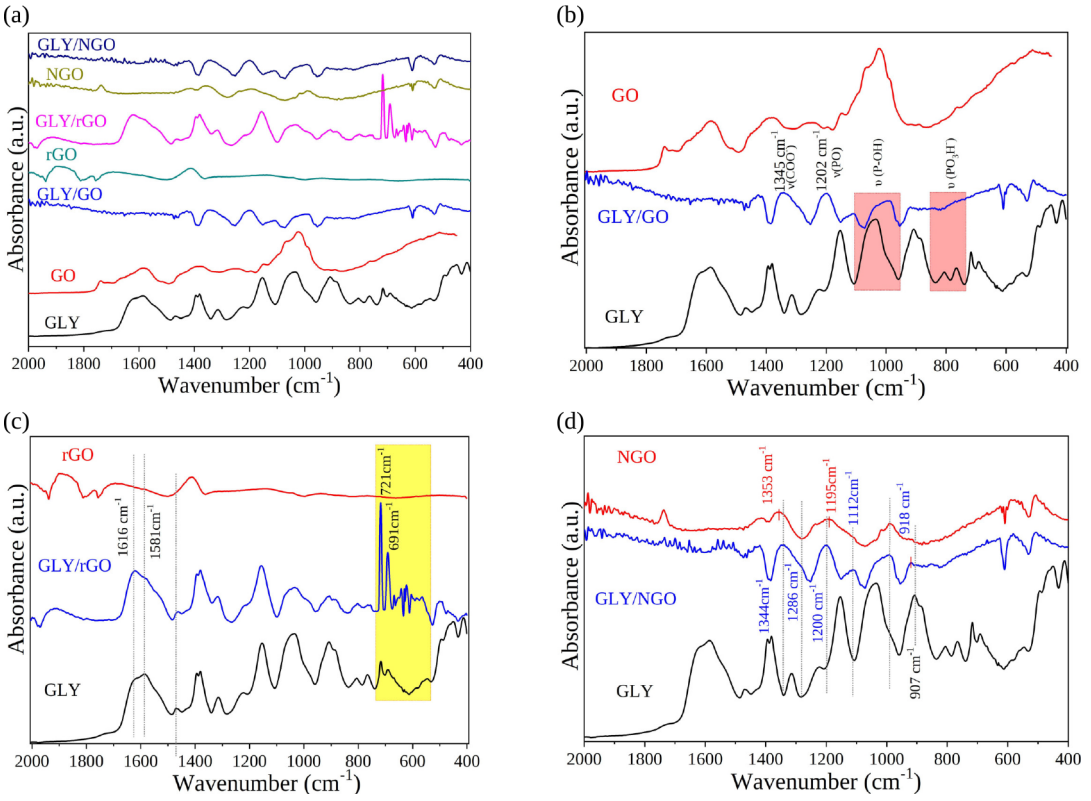

Figure 5. IR studies before and after GLY adsorption: (a) GLY, GO, rGO, and NGO; (b) GO; (c) rGO; and (d) NGO.

increase in the m_T, transitioning from 1.5 μ_B (MVG) to 2.0 μ_B (GLY/MVG).

In case (**3**), encompassing the most stable GLY/NAG and GLY/OAG configurations, it is crucial to contextualize the results appropriately. The graphene substrates with adsorbed N and O atoms act as suppliers of these atoms to the GLY molecule, capturing them and forming new GLY-derived compounds. Consequently, we observe elevated E_{ad} magnitudes (≈−4.051 eV for GLY/NAG and ≈−3.410 eV for GLY/OAG). These values stem from the binding of GLY with the N and O atoms captured from the substrate, in addition to the ensuing interaction between the newly formed compounds and the resultant substrate (PRG). This result is most apparent in the E_{ad} decomposition analysis, revealing the highest E_{int} magnitudes (≈−13.079 eV and ≈−8.462 eV) along with substantial penalties for structural changes in the molecule (≈8.185 eV and ≈3.136 eV) and moderate penalties in the substrate (0.843 and 1.916 eV) for the N and O systems, respectively.

As anticipated, consistent with this energetic outcome, the substantial relative deviation values given by Δd_{av}^{GLY} for both GLY/NAG (−16.463%) and GLY/OAG (−9.135%) reflect the complete transformation of the molecular compound upon capturing the respective substrate atoms. Conversely, the structural changes in the substrate are minimal, as indicated by Δd_{av}^{sub} values of −1.208 and −1.222%, signifying the conversion of NAG and OAG to PRG. Due to the energetic and structural findings, we observe no significant charge transfers between the new GLY-derived compounds and their respective substrates. The m_T behavior is contingent on the molecular types formed upon interaction; for the N system, m_T amounts to 1.0 μ_B, while for the O system, m_T remains null. Examining the interaction of the newly formed compounds (GLY derivatives) with substrates lacking adsorbed atoms (PRG), we find an E_{ad} of −2.328 eV and −0.900 eV, accompanied by $d_{min}^{GLY\text{-}sub}$ values of 2.714 and 2.373 Å for GLY/NAG and GLY/OAG, respectively.

In both case (**2**) and case (**3**), it is crucial to emphasize that the dissociation process and/or the formation of new compounds is more intricate than nondissociative adsorption, such as physisorption or chemisorption. Consequently, the energy values (E_{ad}, E_{int}, E_{dist}^{GLY}) of the most stable GLY/MVG, GLY/NAG, and GLY/OAG conformations are estimated and preceded by the symbol ≈ in the previous discussion. In these instances, E_{ad} is more appropriately termed stabilization energy, resulting from an exceptionally large and additive E_{int} magnitude, along with a substantial penalty in E_{dist}^{GLY} and a moderate penalty in E_{dist}^{sub}. These penalties arise due to molecular dissociation/modification and, to a lesser extent, substrate deformation.

3.2. Experimental Results. *3.2.1. Proposed Mechanism for Glyphosate Adsorption.* The GLY adsorption was further investigated using Fourier-transform infrared (FTIR) and Raman spectroscopies. The FTIR spectra of the various graphene materials before and after GLY adsorption are illustrated in Figure 5 and summarized in Table S6.

The GO spectrum, depicted in Figure 5b, and rGO, Figure 5c, before GLY adsorption, exhibit several bands, as described in our previous work.[55] GO mainly features bands associated with oxygenated groups, such as carbonyls, carboxyls, and epoxides. After reduction with borohydride, these bands practically disappear, as observed in the rGO spectrum, confirming the removal of these groups. The main difference observed in the NGO spectrum is a sharp peak at around 1350 cm^{-1}, characteristic of N-doped graphene.[65]

The GLY spectrum exhibits typical peaks associated with functional groups, including the amine group at 1622 cm^{-1}, carboxylic group at 1394 cm^{-1}, and phosphate group at ≈1040 cm^{-1}, 910 cm^{-1}. The GO spectrum after GLY adsorption, as seen in Figure 5b, contains both GO and GLY bands. The notable change in the spectrum compared to the components before adsorption is the appearance of some prominent new bands at approximately 1345 and 1200 cm^{-1}, commonly attributed to symmetric ν(−COO−) coordinated and ν(−P═O) stretch in phosphates, respectively. Additionally, there is a significant reduction in the band intensities associated with the groups ν(−PO3H−) and ν(−POH) (highlighted by the red squares in Figure 5b).

These results suggest the possibility of forming new bonds, particularly the formation of a complex via carboxylate and the deprotonation of the phosphate group. Given that GO, as a material, presents numerous vacancies in addition to oxygenated groups, we can correlate these results with our theoretical data, which points to the formation of a C−O chemical bond between GLY and MVG (explaining the increase in the band at 1345 cm^{-1}). Furthermore, the theoretical findings indicate that a H atom is lost from the phosphonic group to the vacancy region of the GO, elucidating the reduction in the bands of phosphate groups linked to H and the increase in the band associated with the P═O bond.

The rGO spectrum after GLY adsorption (Figure 5c) predominantly exhibits GLY bands, indicating that GLY, even after filtration and washing, remained on the rGO. This observation suggests a strong interaction between the two components. The initial change observed in the spectrum is the inversion of the intensity ratio between the bands at 1616 and 1581 cm^{-1}, which are related to the asymmetric and symmetric stretching of −NH in amines. This change suggests that when adsorbing on rGO, GLY adopts a conformation where the asymmetric deformation of −NH is more probable, positioning the amine group farther away from the sheet. The most notable change in the spectrum after adsorption is the increased intensity of the bands at 721 and 691 cm^{-1}, attributed to methylene ($-CH_2$) rocking vibration and N−H wag in amines. An increase in peak intensity usually indicates an augmentation in the functional groups associated with these vibrational modes. Comparing with PRG, the theoretical model to which rGO is similar, we observe that the spectroscopic data support the lowest energy conformation (conformation in Figure S6a) observed in the GLY/PRG system, where the amino group and the methyl groups remain further away from the sheet.

On the other hand, the NGO spectrum after GLY adsorption mainly exhibits bands from the graphene material itself, indicating a lower adsorption of GLY compared to other materials. Upon GLY adsorption, some notable changes are observed in the NGO spectrum, including the intensification of two bands: one at 1286 cm^{-1} attributed to stretching of the C−N group and a band at 1112 cm^{-1}, generally attributed to νP̆ OH of the phosphonate. Additionally, two bands attributed to GLY, at 1344 and 907 cm^{-1}, show a blue shift to 1356 and 918 cm^{-1}, respectively. These shifted bands are attributed to the deformation of $-CH_2$ stretching and CCNC skeletal vibration or $-CH_2$ deformation. The down-shifted bands suggest a weakening of the methyl and skeletal bondings, indicating a conformation where these groups are further away

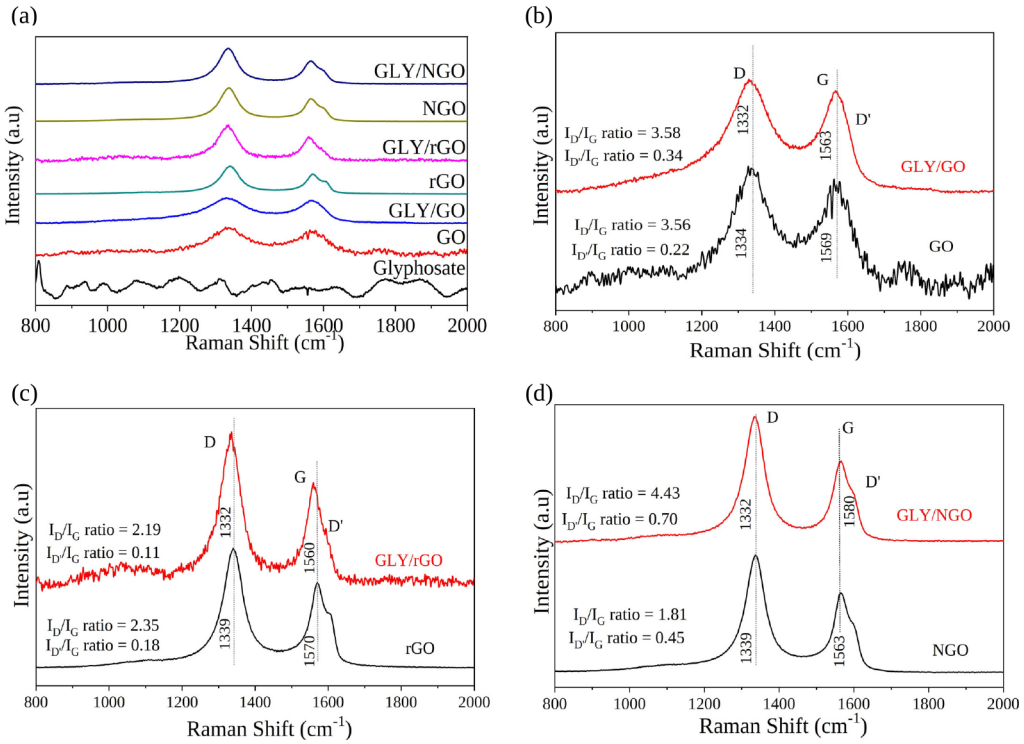

Figure 6. Raman spectra (a) neat-glyphosate, GO, rGO, and NGO before and after GLY adsorption; detailed (b) GO; (c) rGO; and (d) NGO, before and after GLY adsorption.

from the NGO sheet. Moreover, a red shift of the band at 1200 to 1195 cm^{-1}, attributed to the $\nu(-P{=}O)$ stretch in phosphates, suggests that the P═O vibration requires higher energy when GLY is adsorbed, indicating a closer proximity of the phosphate group to the NGO surface. This observation aligns with the most stable conformation for the GLY/NDG system, as depicted in Figure S8a.

3.2.2. Raman Spectroscopy Analysis. Raman spectroscopy serves as a robust characterization technique for analyzing the structure of graphene-based materials. Figure 6 presents the Raman spectra of GLY and various graphene materials before and after GLY adsorption, recorded in the wavenumber range of 800−2000 cm^{-1}. The summarized results are provided in Table S7, and the deconvolution of these spectra is illustrated in Figure S13. For spectral analysis, all spectra were fitted using five functions within the 1000−1800 cm^{-1} range, confirming the presence of D*, D, D″, G, and D′ bands. The D band corresponds to defects or disorder in the carbon lattice, typically associated with sp^3 hybridization, while the G band represents the graphitic or sp^2 carbon bonding. The D* band originates from the vibrations of carbon atoms constrained by functional groups such as oxygen-containing moieties.[66] The attribution of the D″ band is still debated, with main suggestions pointing to the presence of an amorphous lattice, as evidenced by a decrease in its intensity with increased crystallinity and functionalization with small molecules. Lastly, the D′ band corresponds to an intravalley resonance with the G band, exhibiting splits due to impurities, and its intensity is associated with the degree of disorder.

The Raman spectra of GO, rGO, and NGO, presented in Figure 6b−d, respectively, are further examined due to their significant correlation with the structure. All samples' D″ band initially exhibits a similar characteristic, indicating an amorphous lattice.[67] In comparison to GO, both rGO and NGO show a notable decrease in the G band, suggesting a reduction in the sp^2 carbon content and an increased presence of stone wall defects and edge effects.[68] After GLY adsorption, changes in the positions and intensities of many of these bands are observed compared to graphene species before adsorption. The intensity ratio of several bands, including the G and D bands, was calculated to determine the sp^2 domain size and electronic conjugation.

With GLY adsorption, the $I_{D'}/I_G$ ratio increases for GO and NGO while showing a slight decrease for rGO. These results suggest that GLY adsorption introduces additional defects/disorders in GO and NGO, with minimal impact on rGO. These findings align with the data observed in our theoretical calculations and infrared spectroscopy, indicating the introduction of new bonds in the structure of these graphene materials. Another characteristic to be compared is the position of the main bands of graphene materials. For example, D and G bands may shift for two reasons: defects associated with the structure and new functional groups on the sheets. After adsorption, GO and rGO exhibit a red shift, while NGO shows a blue shift for the G band. Based on the variation in the G band position in Raman spectral data, it is speculated that the charge transfer is from the GLY molecule to GO and rGO and from NGO to the GLY molecule. Similar cases have been reported by Ramesha et al.[69] and Das et al.,[70] respectively. These results are consistent with the theoretical data of charge density difference plots for the lowest energy configurations (described in Figure S12), where the charge accumulation is in the graphene material for GLY/MVG and GLY/ODG. For GLY/NDG, the charge accumulation is mostly on GLY.

4. CONCLUSIONS

Our study has comprehensively understood the interactions between the GLY molecule and various graphene-based

substrates. We used an AIMD strategy and DFT calculations to explore the potential energy surface. While PRG has the highest stability, we found that subtle energy differences may lead to punctual defects affecting substrate selection in practical applications. Through individual characterizations and molecular adsorption processes, we identified different interaction behaviors such as physisorption in PRG, NDG, or ODG regions; chemisorption causing molecular dissociation in MVG regions; and complex transformations involving the capture of N and O atoms from adsorbed graphene (NAG or OAG), which resulted in the formation of new GLY-derived compounds. Experimental analysis validated our computational findings, and the FTIR spectra can be directly linked to the most stable conformations obtained from molecular dynamics calculations.

Hence, our analysis, which considers critical properties like adsorption energy, minimum interaction distance, charge variations, structural changes, total magnetic moment, FTIR, and Raman spectroscopies, provides valuable insights into the complex nature of these interactions. The observed behaviors have implications for various applications, ranging from physisorption-dominated scenarios suitable for certain sensing applications to chemisorption-driven processes that may lead to substrate poisoning. Furthermore, capturing N and O atoms by GLY and the resulting formation of new compounds offer possibilities for various chemical GLY transformations. In summary, this study enhances our fundamental knowledge of GLY-graphene interactions, directs future experimental investigations, and emphasizes the multifaceted nature of analyte-substrate systems.

AUTHOR INFORMATION

Corresponding Author

Celso Ricardo Caldeira Rêgo − *Institute of Nanotechnology Hermann-von-Helmholtz-Platz, Karlsruhe Institute of Technology, 76021 Karlsruhe, Germany;* orcid.org/0000-0003-1861-2438; Email: celso.rego@kit.edu

Authors

Wanderson S. Araújo − *Department of Physics, Federal University of Pelotas, Pelotas, Rio Grande do Sul 96010-900, Brazil*

Diego Guedes-Sobrinho − *Chemistry Department, Federal University of Paraná, Curitiba, Paraná 81531-980, Brazil;* orcid.org/0000-0002-3313-2822

Alexandre Cavalheiro Dias − *Institute of Physics and International Center of Physics, University of Brasília, Brasília, Federal District 70919-970, Brazil;* orcid.org/0000-0001-5934-8528

Isadora Rodrigues do Couto − *Department of Chemistry, Federal University of Santa Maria, Santa Maria, Rio Grande do Sul 97105-900, Brazil*

José Rafael Bordin − *Department of Physics, Federal University of Pelotas, Pelotas, Rio Grande do Sul 96010-900, Brazil;* orcid.org/0000-0002-8025-6529

Carolina Ferreira de Matos − *Department of Chemistry, Federal University of Santa Maria, Santa Maria, Rio Grande do Sul 97105-900, Brazil;* orcid.org/0000-0001-8134-1656

Maurício Jeomar Piotrowski − *Department of Physics, Federal University of Pelotas, Pelotas, Rio Grande do Sul 96010-900, Brazil;* orcid.org/0000-0003-3477-4437

Notes

The authors declare no competing financial interest.

ACKNOWLEDGMENTS

Authors thank the Rio Grande do Sul Research Foundation − FAPERGS (J.R.B. grant number 21/2551-0002024-5), the Federal District Research Support Foundation (FAPDF, grants 00193-00001817/2023-43 and 00193-00002073/2023-84), the National Council for Scientific and Technological Development − CNPq (M.J.P. grant number 307345/2021-1, J.R.B. and C.F.M. grant numbers 405479/2023-9 and 403427/2021-5, J.R.B. grant number 304958/2022−0, A.C.D. grant number 408144/2022-0), the Coordination for Improvement of Higher Level Education − CAPES (finance Code 001) for the financial support. C.R.C.R. thanks the German Federal Ministry of Education and Research (BMBF) for financial support of the project Innovation-Platform MaterialDigital (www.materialdigital.de) through project funding FKZ number: 13XP5094A. Part of this work was performed on the HoreKa supercomputer funded by the Ministry of Science, Research, and the Arts Baden-Württemberg and by the Federal Ministry of Education and Research. The authors also thank the infrastructure provided to our computer cluster by the Department of Physics from the Federal University of Pelotas. This work also used resources of the "Centro Nacional de Processamento de Alto Desempenho em São Paulo" (CENAPAD−SP, UNICAMP/FINEP - MCTI), projects 897 and 570; of the "Centro Nacional de Supercomputação (CESUP−UFRGS)"; of the Lobo Carneiro HPC (NACAD) at the Federal University of Rio de Janeiro (UFRJ) for resources for project 133; of the CIMATEC SENAI at Salvador − BA, for their partnership and support through the Ogun Supercomputer; and of the "Laboratório Central de Processamento de Alto Desempenho" (LCPAD) financed by FINEP through CT-INFRA/UFPR projects.

ABBREVIATIONS

DFT, Density Functional Theory; PBE, Perdew−Burke−Ernzerhof; D3, dispersion correction; VASP, Vienna Ab initio Simulation Package; PAW, projected augmented wave; FTIR, Fourier-transform infrared; BZ, Brillouin zone; GLY, Glyphosate

REFERENCES

(1) Nechaev, V. I. Innovative Development in Agriculture. In *Complex Systems: Innovation and Sustainability in the Digital Age: Volume 1*; Bogoviz, A. V., Ed.; Springer International Publishing: Cham, 2020; pp 595−603.

(2) da Silva, F. T.; Baierle, I. C.; de F Correa, R. G.; Sellitto, M. A.; Peres, F. A. P.; Kipper, L. M. Open Innovation in Agribusiness: Barriers and Challenges in the Transition to Agriculture 4.0. *Sustainability* **2023**, *15*, 8562.

(3) Carvalho, F. P. Pesticides, environment, and food safety. *Food and Energy Security* **2017**, *6*, 48−60.

(4) Duke, S. O. The history and current status of glyphosate. *Pest. Manag. Sci.* **2018**, *74*, 1027−1034.

(5) Fuchs, R.; Alexander, P.; Brown, C.; Cossar, F.; Henry, R. C.; Rounsevell, M. Why the US−China trade war spells disaster for the Amazon. *Nature* **2019**, *567*, 451−454.

(6) *Sistema de Agrotóxicos Fitossanitários. Ministério da Agricultura Pecuária e Abastecimento BRASIL*. http://agrofit.agricultura.gov.br/agrofit_cons/principal_agrofit_cons, 2020.

(7) Solomon, K.; Thompson, D. Ecological risk assessment for aquatic organisms from over water uses of glyphosate. *J. Toxicol. Environ. Health B* **2003**, *6*, 289−324.

(8) Kniss, A. R. Long-term trends in the intensity and relative toxicity of herbicide use. *Nature Comm.* **2017**, *8*, 14865.

(9) Zyoud, S. H.; Waring, W. S.; Al-Jabi, S. W.; Sweileh, W. M. Global research production in glyphosate intoxication from 1978 to 2015: a bibliometric analysis. *Human Exp. Toxic.* **2017**, *36*, 997−1006.

(10) Souza, M. F.; Langaro, A. C.; Passos, A. B. R. J.; Lins, H. A.; Silva, T. S.; Mendonça, V.; Silva, A. A.; Silva, D. V. Adsorption mechanisms of atrazine isolated and mixed with glyphosate formulations in soil. *PLoS One* **2020**, *15*, No. e0242350.

(11) Yang, Y.; Deng, Q.; Yan, W.; Jing, C.; Zhang, Y. Comparative study of glyphosate removal on goethite and magnetite: adsorption and photo-degradation. *Chem. Eng. J.* **2018**, *352*, 581−589.

(12) Bruggen, A. H. C. V.; He, M. M.; Shin, K.; Mai, V.; Jeong, K. C.; Finckh, M. R.; Morris, J. G. J. Environmental and health effects of the herbicide glyphosate. *Sci. Total Environ.* **2018**, *616−617*, 255−268.

(13) Lima, I. B.; Boëchat, I. G.; Fernandes, M. D.; Monteiro, J. A. F.; Rivaroli, L.; Gücker, B. Glyphosate pollution of surface runoff, stream water, and drinking water resources in Southeast Brazil. *Environmental Science and Pollution Research* **2023**, *30*, 27030−27040.

(14) Gomes, M. P.; Brito, J. C. M.; Vieira, F.; Kitamura, R. S. A.; Juneau, P. Emerging Contaminants in Streams of Doce River Watershed, Minas Gerais, Brazil. *Front. Environ. Sci.* **2022**, *9*, No. 801599, DOI: 10.3389/fenvs.2021.801599.

(15) Manas, F. L.; Peralta, J. R.; Ovando, H. G.; Weyers, A.; Ugnia, L.; Cid, M. G.; Larripa, I.; Gorla, N. Genotoxicity of glyphosate assessed by the comet assay and cytogenetic tests. *Environ. Toxicol. Pharmacol.* **2009**, *28*, 37−41.

(16) Pu, Y.; Yang, J.; Chang, L.; Qu, Y.; Wang, S.; Zhang, K.; Xiong, Z.; Zhang, J.; Tan, Y.; Wang, X.; Fujita, Y.; Ishima, T.; Wan, D.; Hwang, S. H.; Hammock, B. D.; Hashimoto, K. Maternal glyphosate exposure causes autism-likebehaviors in offspring through increased expression of soluble epoxide hydrolase. *Proc. Natl. Acad. Sci. U.S.A.* **2020**, *117*, 11753−11759.

(17) European Food Safety Authority (EFSA). Conclusion on the peer review of the pesticide risk assessment of the active substance glyphosate. *EFSA J.* **2015**, *13*, 4302 DOI: 10.2903/j.efsa.2015.4302.

(18) Tarazona, J. V.; Court-Marques, D.; Tiramani, M.; Reich, H.; Pfeil, R.; Istace, F.; Crivellente, F. Glyphosate toxicity and carcinogenicity: a review of the scientific basis of the European Union assessment and its differences with IARC. *Arch. Toxicol.* **2017**, *91*, 2723−2743.

(19) Rana, I.; Nguyen, P. K.; Rigutto, G.; Louie, A.; Lee, J.; Smith, M. T.; Zhang, L. Mapping the key characteristics of carcinogens for glyphosate and its formulations: A systematic review. *Chemosphere* **2023**, *339*, No. 139572.

(20) Ferrante, M.; Rapisarda, P.; Grasso, A.; Favara, C.; Oliveri Conti, G. Glyphosate and environmental toxicity with One Health approach, a review. *Environmental Research* **2023**, *235*, No. 116678.

(21) Brovini, E. M.; Cardoso, S. J.; Quadra, G. R.; Vilas-Boas, J. A.; Paranaíba, J. R.; Pereira, R. D. O.; Mendonça, R. F. Glyphosate concentrations in global freshwaters: are aquatic organisms at risk? *Environmental Science and Pollution Research* **2021**, *28*, 60635−60648.

(22) Casassus, B. EU allows use of controversial weedkiller glyphosate for 10 more years. *Nature* **2023**, DOI: 10.1038/d41586-023-03589-z.

(23) Ogunbiyi, O. D.; Akamo, D. O.; Oluwasanmi, E. E.; Adebanjo, J.; Isafiade, B. A.; Ogunbiyi, T. J.; Alli, Y. A.; Ayodele, D. T.; Oladoye, P. O. Glyphosate-based herbicide: Impacts, detection, and removal strategies in environmental samples. *Groundwater for Sustainable Development* **2023**, *22*, No. 100961.

(24) Mazuryk, J.; Klepacka, K.; Kutner, W.; Sharma, P. S. Glyphosate Separating and Sensing for Precision Agriculture and Environmental Protection in the Era of Smart Materials. *Environ. Sci. Technol.* **2023**, *57*, 9898−9924.

(25) Zelenkova, N. F.; Vinokurova, N. G. Determination of Glyphosate and Its Biodegradation Products by Chromatographic Methods. *J. Analyt. Chem.* **2008**, *63*, 871−874.

(26) Noori, J. S.; Mortensen, J.; Geto, A. Recent Development on the Electrochemical Detection of Selected Pesticides: A Focused Review. *Sensors* **2020**, *20*, 2221.

(27) Geana, E.-I.; Baracu, A. M.; Stoian, M. C.; Brincoveanu, O.; Pachiu, C.; Dinu, L. A. Hybrid nanomaterial-based indirect electrochemical sensing of glyphosate in surface water: a promising approach for environmental monitoring. *Environmental Science: Processes & Impacts* **2023**, *25*, 2057−2066.

(28) Gerber, I. C.; Serp, P. A Theory/Experience Description of Support Effects in Carbon-Supported Catalysts. *Chem. Rev.* **2020**, *120*, 1250−1349.

(29) de Ridder, D. J.; Villacorte, L.; Verliefde, A. R. D.; Verberk, J. Q. J. C.; Heijman, S. G. J.; Amy, G. L.; van Dijk, J. C. Modeling equilibrium adsorption of organic micropollutants onto activated carbon. *Water Res.* **2010**, *44*, 3077−3086.

(30) Mayakaduwa, S. S.; Kumarathilaka, P.; Herath, I.; Ahmad, M.; Al-Wabel, M.; Ok, Y. S.; Usman, A.; Abduljabbar, A.; Vithanage, M. Equilibrium and kinetic mechanisms of woody biochar on aqueous glyphosate removal. *Chemosphere* **2016**, *144*, 2516−2521.

(31) Diel, J. C.; Franco, D. S. P.; Nunes, I. S.; Pereira, H. A.; Moreira, K. S.; Burgo, T. A. L.; Foletto, E. L.; Dotto, G. L. Carbon nanotubes impregnated with metallic nanoparticles and their application as an adsorbent for the glyphosate removal in an aqueous matrix. *J. Environ. Chem. Eng.* **2021**, *9*, No. 105178.

(32) Sen, K.; Chattoraj, S. 5 - A comprehensive review of glyphosate adsorption with factors influencing mechanism: Kinetics, isotherms, thermodynamics study. In *Intelligent Environmental Data Monitoring for Pollution Management*; Bhattacharyya, S.; Mondal, N. K.; Platos, J.; Snasel, V.; Kromer, P., Eds.; Intelligent Data-Centric Systems; Academic Press, 2021; pp 93−125.

(33) Tewari, C.; Tatrari, G.; Kumar, S.; Pathak, M.; Rawat, K. S.; Kim, Y. N.; Saha, B.; Jung, Y. C.; Mukhopadhyay, P.; Sahoo, N. G. Can graphene-based composites and membranes solve current water purification challenges - a comprehensive review. *Desalination* **2023**, *567*, No. 116952.

(34) Ighalo, J. O.; Ajala, O. J.; Adeniyi, A. G.; Babatunde, E. O.; Ajala, M. A. Ecotoxicology of glyphosate and recent advances in its mitigation by adsorption. *Environ. Sci. Pollut. Research* **2021**, *28*, 2655−2668.

(35) Novoselov, K. S.; Geim, A. K.; Morozov, S. V.; Jiang, D.; Zhang, Y.; Dubonos, S. V.; Grigorieva, I. V.; Firsov, A. A. Electric Field Effect in Atomically Thin Carbon Films. *Science* **2004**, *306*, 666−669.

(36) Leão, M. B.; Bordin, J. R.; de Matos, C. F. Specific Surface Area Versus Adsorptive Capacity: an Application View of 3D Graphene-Based Materials for the Removal of Emerging Water Pollutants. *Water, Air, & Soil Pollution* **2023**, *234*, 136.

(37) He, Q.; Wu, S.; Yin, Z.; Zhang, H. Graphene-based electronic sensors. *Chem. Sci.* **2012**, *3*, 1764−1772.
(38) Krasheninnikov, A. V.; Lehtinen, P. O.; Foster, A. S.; Pyykkö, P.; Nieminen, R. M. Embedding Transition-Metal Atoms in Graphene: Structure, Bonding, and Magnetism. *Phys. Rev. Lett.* **2009**, *102*, No. 126807.
(39) Rêgo, C. R. C.; Tereshchuk, P.; Oliveira, L. N.; Silva, J. L. F. D. Graphene-supported small transition-metal clusters: A density functional theory investigation within van der Waals corrections. *Phys. Rev. B* **2017**, *95*, No. 235422.
(40) Yamaguchi, N. U.; Bergamasco, R.; Hamoudi, S. Magnetic $MnFe_2O_4$ graphene hybrid composite for efficient removal of glyphosate from water. *Chem. Eng. J.* **2016**, *295*, 391−402.
(41) Marin, P.; Bergamasco, R.; Módenes, A. N.; Paraiso, P. R.; Hamoudi, S. Synthesis and characterization of graphene oxide functionalized with $MnFe_2O_4$ and supported on activated carbon for glyphosate adsorption in fixed bed column. *Proc. Saf. Environ. Protection* **2019**, *123*, 59−71.
(42) Perea-Ramírez, R.; Vargas, L. I.; Domínguez, Z.; Salas-Reyes, M.; Matus, M. H.; Galvan, M. Theoretical study of the adsorption of substituted guaiacol and catechol radicals on a graphite surface. *Electrochim. Acta* **2017**, *242*, 66−72.
(43) Jaimes, R.; Cervantes-Alcalá, R.; García-García, W.; Miranda-Hernández, M. Ab initio computational modeling of the electrochemical reactivity of quinones on gold and glassy carbon electrodes. *Electrochim. Acta* **2018**, *284*, 108−118.
(44) Sousa, K. A. P.; Morawski, F. M.; de Campos, C. E. M.; Parreira, R. L. T.; Piotrowski, M. J.; Nagurniak, G. R.; Jost, C. L. Electrochemical, theoretical, and analytical investigation of the phenylurea herbicide fluometuron at a glassy carbon electrode. *Electrochim. Acta* **2022**, *408*, No. 139945.
(45) Hohenberg, P.; Kohn, W. Inhomogeneous electron gas. *Phys. Rev.* **1964**, *136*, B864.
(46) Kohn, W.; Sham, L. J. Self-consistent equations including exchange and correlation effects. *Phys. Rev.* **1965**, *140*, A1133.
(47) Perdew, J. P.; Burke, S.; Ernzerhof, M. Generalized Gradient Approximation Made Simple. *Phys. Rev. B* **1996**, *77*, 3865−3868.
(48) Rêgo, C. R. C.; Oliveira, L. N.; Tereshchuk, P.; Da Silva, J. L. F. Comparative Study of van der Waals Corrections to the Bulk Properties of Graphite. *J. Phys.: Condens. Matter* **2015**, *27*, No. 415502.
(49) Rêgo, C. R. C.; Oliveira, L. N.; Tereshchuk, P.; Silva, J. L. F. D. Corrigendum: Comparative study of van der Waals corrections to the bulk properties of graphite (2015 J. Phys.: Condens. Matter. 27415502). *J. Phys.: Condens. Matter* **2016**, *28*, No. 129501.
(50) Grimme, S. Semiempirical GGA-type density functional constructed with a long-range dispersion correction. *J. Comput. Chem.* **2006**, *27*, 1787−1799.
(51) Blöchl, P. E. Projector augmented-wave method. *Phys. Rev. B* **1994**, *50*, 17953.
(52) Kresse, G.; Hafner, J. Ab initio molecular dynamics for open-shell transition metals. *Phys. Rev. B* **1993**, *48*, 13115−13126.
(53) Kresse, G.; Furthmüller, J. Efficient iterative schemes for *ab initio* total-energy calculations using a plane-wave basis set. *Phys. Rev. B* **1996**, *54*, 11169.
(54) Koelling, D. D.; Harmon, B. N. A technique for relativistic spin-polarised calculations. *J. Phys. C Solid State Phys.* **1977**, *10*, 3107.
(55) Mehl, H.; Matos, C. F.; Neiva, E. G. C.; Domingues, S. H.; Zarbin, A. J. G. The effect of variation of reactional parameters in the preparation of graphene by oxidation and reduction of graphite. *Quim. Nova* **2014**, 1639−1645.
(56) Sun, H.; Wang, Y.; Liu, S.; Ge, L.; Wang, L.; Zhu, Z.; Wang, S. Facile synthesis of nitrogen doped reduced graphene oxide as a superior metal-free catalyst for oxidation. *Chem. Commun.* **2013**, *49*, 9914.
(57) Knuuttila, P.; Knuuttila, H. The Crystal and Molecular Structure of N-(Phosphonomethyl)-glycine (Glyphosate). *Acta Chem. Scand. B* **1979**, *33*, 623−626.
(58) Holanda, R. O.; da Silva, C. B.; Vasconcelos, D. L.M.; Freire, P. T. C. High pressure Raman spectra and DFT calculation of glyphosate. *Spectrochim. Acta Part A: Mol. Biomol. Spectr.* **2020**, *242*, No. 118745.
(59) Liua, B.; Donga, L.; Yua, Q.; Lia, X.; Wub, F.; Tana, Z.; Luo, S. Thermodynamic Study on the Protonation Reactions of Glyphosate in Aqueous Solution: Potentiometry, Calorimetry and NMR spectroscopy. *J. Phys. Chem. B* **2016**, *120*, 2132−2137.
(60) Padmanabhan, H.; Nanda, B. R. K. Intertwined lattice deformation and magnetism in monovacancy graphene. *Phys. Rev. B* **2016**, *93*, No. 165403.
(61) Elias, D. C.; Nair, R. R.; Mohiuddin, T. M. G.; Morozov, S. V.; Blake, P.; Halsall, M. P.; Ferrari, A. C.; Boukhvalov, D. W.; Katsnelson, M. I.; Geim, A. K.; Novoselov, K. S. Control of graphene's properties by reversible hydrogenation: evidence for graphene. *Science* **2009**, *323*, 610−613.
(62) Thrower, P. A.; Mayer, R. M. Point defects and self-diffusion in graphite. *Phys. Stat. Sol. (a)* **1978**, *47*, 11−37.
(63) Mehmood, F.; Pachter, R.; Lu, W.; Boeckl, J. J. Adsorption and Diffusion of Oxygen on Single-Layer Graphene with Topological Defects. *J. Phys. Chem. C* **2013**, *117*, 10366−10374.
(64) Zhu, X.; Liu, K.; Lu, Z.; Xu, Y.; Qi, S.; Zhang, G. Effect of oxygen atoms on graphene: Adsorption and doping. *Phys. E* **2020**, *117*, No. 113827.
(65) Lazar, P.; Mach, R.; Otyepka, M. Spectroscopic Fingerprints of Graphitic, Pyrrolic, Pyridinic, and Chemisorbed Nitrogen in N-Doped Graphene. *J. Phys. Chem. C* **2019**, *123*, 10695−10702.
(66) Lee, A. Y.; Yang, K.; Anh, N. D.; Park, C.; Lee, S. M.; Lee, T. G.; Jeong, M. S. Raman study of D∗ band in graphene oxide and its correlation with reduction. *Appl. Surf. Sci.* **2021**, *536*, No. 147990.
(67) Hartmann, S. J.; Iurchenkova, A. A.; Kallio, T.; Fedorovskaya, E. O. Electrochemical Properties of Nitrogen and Oxygen Doped Reduced Graphene Oxide. *Energies* **2020**, *13*, 312.
(68) Tiwari, S. K.; Pandey, S. K.; Pandey, R.; Wang, N.; Bystrzejewski, M.; Mishra, Y. K.; Zhu, Y. Stone-Wales Defect in Graphene. *Small* **2023**, *19*, No. 2303340.
(69) Das, B.; Voggu, R.; Rout, C. S.; Rao, C. N. R. Changes in the electronic structure and properties of graphene induced by molecular charge-transfer. *Chem. Commun.* **2008**, 5155−5157.
(70) Ramesha, G.; Vijaya Kumara, A.; Muralidhara, H.; Sampath, S. Graphene and graphene oxide as effective adsorbents toward anionic and cationic dyes. *J. Colloid Interface Sci.* **2011**, *361*, 270−277.